Streamline topology of steady axisymmetric vortex breakdown in a cylinder with co- and counter-rotating end-covers

By MORTEN BRØNS[1], LARS KØLLGAARD VOIGT[1,2]
AND JENS NØRKÆR SØRENSEN[2]

[1] Department of Mathematics, Technical University of Denmark, Building 303,
DK-2800 Lyngby, Denmark

[2] Department of Energy Engineering, Technical University of Denmark, Building 404,
DK-2800 Lyngby, Denmark

Using a combination of bifurcation theory for two-dimensional dynamical systems and numerical simulations, we systematically determine the possible flow topologies of the steady vortex breakdown in axisymmetric flow in a cylindrical container with rotating end-covers. For fixed values of the ratio of the angular velocities of the covers in the range from -0.02 to 0.05, bifurcations of recirculating bubbles under variation of the aspect ratio of the cylinder and the Reynolds number are found. Bifurcation curves are determined by a simple fitting procedure of the data from the simulations. For the much studied case of zero rotation ratio (one fixed cover) a complete bifurcation diagram is constructed. Very good agreement with experimental results is obtained, and hitherto unresolved details are determined in the parameter region where up to three bubbles exist. For non-zero rotation ratios the bifurcation diagrams are found to change dramatically and give rise to other types of bifurcations.

1. Introduction

The flow in a closed cylindrical container with one fixed and one rotating end-cover has long been a standard configuration for the study of vortex breakdown. Experimental investigations by Vogel (1968), Ronnenberg (1977), and Escudier (1984) show that in the steady regime up to three recirculation zones or 'bubbles' can exist close to the axis of the central vortex. Spohn, Mory & Hopfinger (1993) found an even richer set of flow structures in a flow where the fixed cover is replaced by a free surface. Numerous numerical simulations assuming the flow is axisymmetric (e.g. Sørensen & Loc 1989; Lopez 1990; Sørensen & Christensen 1995) reproduce the experiments well, although the axisymmetry is a matter of some controversy (Spohn, Mory & Hopfinger 1998; Sotiropoulos & Ventikos 1998). While the first transition to unsteady flow is via a Hopf bifurcation (Lopez & Perry 1992; Sørensen & Christensen 1995) it was shown numerically by Gelfat, Bar-Yoseph & Solan (1996*a*) and Tsitverblit (1993) that the creation of recirculation bubbles in the steady regime is not caused by an instability but is the result of a smooth topological change of the flow field. Roesner (1989), Bar-Yoseph, Solan & Roesner (1990), Gelfat, Bar-Yoseph & Solan (1996*b*), and Jahnke & Valentine (1998) have investigated the effect of co- and counter-rotation of the otherwise fixed cover of the cylinder. The flow structures

and the stability of the flow turns out to be remarkably sensitive to changes in the rotation ratio of the two covers.

In the present paper we apply a dynamical systems approach to describe the creation and transformation of the recirculating structures in the steady domain under variation of three parameters: the Reynolds number Re, the aspect ratio h of the cylinder, and the ratio of the angular velocities of the two covers, γ. The use of dynamical systems theory to qualitatively describe streamline patterns has a long history, for basic ideas see for example Hunt *et al.* (1978) and the reviews by Tobak & Peake (1982) and Perry & Chong (1987). In particular, bifurcation theory has been used to describe changes in patterns, for example in flows close to a wall (Bakker 1991; Hartnack 1999), flows close to free and viscous interfaces (Brøns 1994), and general flows away from boundaries (Brøns & Hartnack 1999).

It is important to realize that the creation and change of patterns in fluids can be attributed to bifurcations at different levels of description. When the Navier–Stokes equations are considered as a dynamical system in some infinite-dimensional space of velocity fields, bifurcation can occur under variation of parameters, and the streamline pattern of the bifurcating solution can be topologically distinct from the old one. For example, the creation of convection cells in a Rayleigh–Bénard flow is a pitchfork bifurcation in this sense from the zero-flow solution which loses stability in the bifurcation.

No such bifurcations occur in the present problem in the parameter range considered. Here, there is a unique stable steady velocity field $v = v(Re, h, \gamma)$, but as the parameters are varied bifurcations in the streamline pattern, i.e. for the ordinary differential equations $\dot{x} = v$, occur. Due to axisymmetry this reduces to a two-dimensional system, and it is the bifurcations of these equations considered as a dynamical system that we will explore.

The theoretical basis for the present analysis is the topological classification of axisymmetric patterns by Brøns (1999) which gives a list of possible bifurcations of the patterns as external parameters are varied. The analysis relies on normal form transformations which simplify the differential equations for the streamlines considerably. We perform numerical computations using the finite-difference code described by Sørensen & Loc (1989) and by simple fitting procedures get the bifurcation sets from a quite small number of simulations. For the rotation ratio $\gamma = 0$, that is, one fixed cover, we compare with experiments by Escudier (1984) and Roesner (1989) and get very good agreement for the regime with up to two bubbles. We also show that the regime with three bubbles is larger than previously assumed and resolve the quite complicated bifurcation diagram in this region.

For small non-zero rotation ratios we also find the bifurcation diagrams with up to two bubbles and get an overview of the way the diagrams vary with this parameter.

Dynamical systems have previously been used only to give a qualitative description of streamline topologies. To the authors' knowledge this is the first attempt to link the abstract classification of streamline bifurcations with a specific flow to obtain quantitative information. This approach may be useful for other flows where the topology of coherent structures is of interest.

2. Formulation of the problem

We consider viscous, incompressible, axisymmetric flow in a cylinder of height H and radius R. The bottom and top covers rotate with constant angular velocities

Ω_1, Ω_2, respectively. Three dimensionless quantities characterizing the problem are

$$Re = \frac{\Omega_1 R^2}{v}, \quad h = \frac{H}{R}, \quad \gamma = \frac{\Omega_2}{\Omega_1}, \tag{2.1}$$

where v is the kinematic viscosity of the fluid. The flow is described using cylindrical coordinates (r, θ, z) with corresponding velocity $\boldsymbol{v} = (u, v, w)$ depending only on r, z. A stream function $\psi(r, z)$ can be defined such that

$$u = \frac{1}{r}\frac{\partial \psi}{\partial z}, \quad w = -\frac{1}{r}\frac{\partial \psi}{\partial r}. \tag{2.2}$$

Hence, the velocity field can be described by the scalar functions ψ and v. The latter gives the swirling motion of the fluid, while the iso-curves of ψ, from (2.2), are the intersections of the physical stream-surfaces with any meridional plane. Here we are concerned with ψ only. In a steady flow iso-curves of ψ can be found experimentally by letting a meridional sheet of light pass through the fluid in which reflecting particles are released. For simplicity, we will denote the iso-curves of ψ streamlines, even if the real physical streamlines are spirals winding around the axis.

To obtain ψ we use the finite-difference code developed at LIMSI/CNRS in France, (Daube *et al.* 1985; Sørensen & Loc 1989). The code uses transport equations for azimuthal components of vorticity and velocity. Letting ω denote the azimuthal component of $\boldsymbol{\omega} = \nabla \times \boldsymbol{v}$, the Poisson equation for the stream function is given by

$$\frac{\partial^2 \psi}{\partial z^2} + \frac{\partial^2 \psi}{\partial r^2} - \frac{1}{r}\frac{\partial \psi}{\partial r} = r\omega. \tag{2.3}$$

The azimuthal velocity and vorticity transport equations are given by

$$\frac{\partial v}{\partial t} + \frac{\partial}{\partial r}(uv) + \frac{\partial}{\partial z}(wv) - \frac{2}{r}uv = \frac{1}{Re}\left[\frac{\partial}{\partial r}\left(\frac{1}{r}\frac{\partial(rv)}{\partial r}\right) + \frac{\partial^2 v}{\partial z^2}\right], \tag{2.4a}$$

$$\frac{\partial \omega}{\partial t} + \frac{\partial}{\partial r}(u\omega) + \frac{\partial}{\partial z}(w\omega) - \frac{1}{r}\frac{\partial}{\partial z}(v^2) = \frac{1}{Re}\left[\frac{\partial}{\partial r}\left(\frac{1}{r}\frac{\partial(r\omega)}{\partial r}\right) + \frac{\partial^2 \omega}{\partial z^2}\right]. \tag{2.4b}$$

In these non-dimensional equations, length and time have been scaled with R and Ω_1 respectively. For a closed cylinder with rotating top and bottom the following boundary conditions apply:

centre axis, $r = 0, 0 \leqslant z \leqslant h$:

$$\psi = u = \omega = \frac{\partial \psi}{\partial r} = 0, \, v = 0, \, \frac{\partial^2 \psi}{\partial r^2} = -w; \tag{2.5}$$

cylinder wall, $r = 1, 0 \leqslant z \leqslant h$:

$$\psi = u = w = \frac{\partial \psi}{\partial r} = 0, \, v = 0, \, \frac{\partial^2 \psi}{\partial r^2} = r\omega; \tag{2.6}$$

rotating lid, $z = 1, 0 \leqslant r \leqslant 1$:

$$\psi = u = w = \frac{\partial \psi}{\partial z} = 0, \, v = \gamma r, \, \frac{\partial^2 \psi}{\partial z^2} = r\omega; \tag{2.7}$$

rotating bottom, $z = 0, 0 \leqslant r \leqslant 1$:

$$\psi = u = w = \frac{\partial \psi}{\partial z} = 0, \, v = r, \, \frac{\partial^2 \psi}{\partial z^2} = r\omega. \tag{2.8}$$

The transport equations are discretized by a second-order central difference scheme. The Poisson equation is discretized to fourth-order accuracy using three-point Hermitean expressions for the derivatives of the stream function. The boundary conditions were implemented by using Taylor expansions into the flow domain. The transport equations were solved alternately with the Poisson equation. For each equation, every iteration was split into two steps, one step for the z-direction and one step for the r-direction, employing the ADI technique. Further details about the numerical implementation, including references, can be found in Sørensen & Loc (1989). By investigating different grid sizes, a grid resolution of $\Delta r = \Delta z = 0.01$ was found to be sufficient for analysing the parameter ranges in our work (see §4.2). Hence a larger computational effort is needed for higher values of h.

Using the code, we obtain steady states by simulating until transients have died out. We accept a state as being steady if the relative change of ψ at the (arbitrary) grid point $(50, 50)$ has not been more than 10^{-8} for at least 100 time-step iterations. In most cases the criterion was fulfilled for at least twice as many iterations. The six distinct flow topologies found (excluding the degenerate configurations which occur at a bifurcation) are shown in figure 1. In cases B and C it makes sense to distinguish between subcases which from a strict topological point of view are identical. We return to this matter in §4.1.

Our goal is to obtain a partition of the (Re, h, γ) parameter space into regions, separated by bifurcation sets, where the topology of the flow is of the same type. In the next section we outline the theory describing the possible qualitative structures of the bifurcation sets.

3. Topology of axisymmetric flow

The basic idea in a dynamical systems or topological approach to fluid mechanics is to analyse the trajectories of the ordinary differential equations $\dot{x} = v$, where v is a velocity field, as these curves are by definition the streamlines. Incompressible axisymmetric flow has been analysed from this point of view by Brøns (1999), and we review the main results here.

Since the axis is a streamline, and due to axisymmetry, we have the boundary conditions

$$\psi = 0, \quad \frac{\partial^{2n-1}\psi}{\partial r^{2n-1}} = 0 \quad \text{for} \quad r = 0 \quad \text{and all } n \in \mathbb{N}. \tag{3.1}$$

This makes it convenient to use $\rho = \frac{1}{2}r^2$ as a radial variable. The differential equations for the iso-curves of ψ become

$$\dot{\rho} = \frac{\partial \psi}{\partial z}, \quad \dot{z} = -\frac{\partial \psi}{\partial \rho}, \tag{3.2}$$

which is a Hamiltonian system with total energy ψ.

To study the flow close to a given point on the axis, we choose the point to be the origin and introduce the Taylor expansion

$$\psi = \sum_{n+m=0}^{\infty} a_{nm}\rho^n z^m. \tag{3.3}$$

The boundary conditions (3.1) are satisfied if

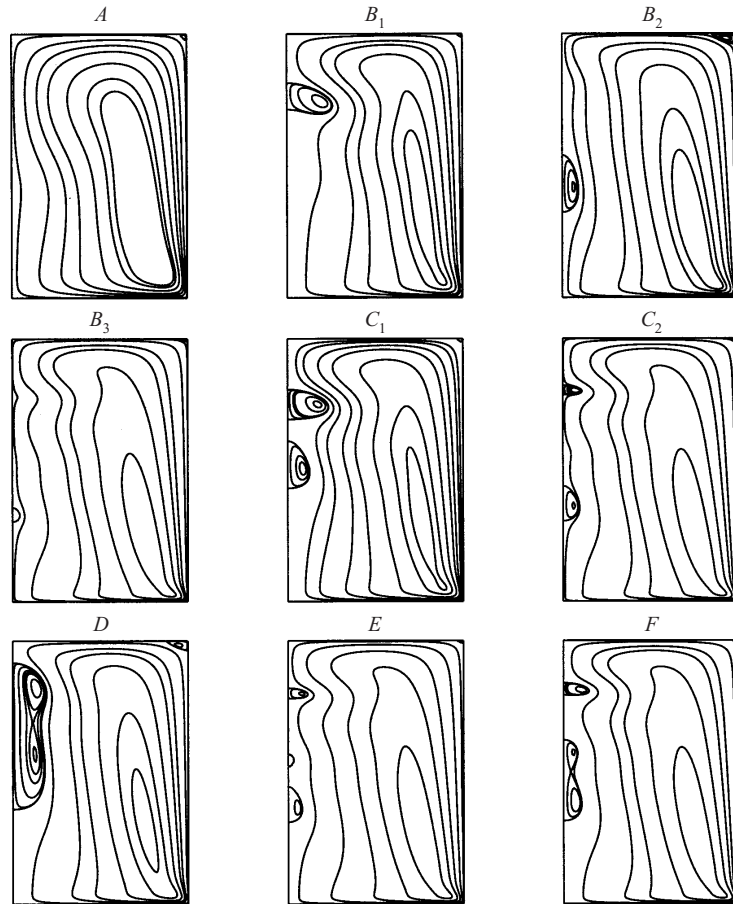$$a_{0m} = 0, \quad m = 0, 1, \dots . \tag{3.4}$$

FIGURE 1. Typical representations of the flow topologies (iso-curves of ψ) found in the steady domain. The bottom cover rotates with angular velocity Ω_1 and the top cover with angular velocity Ω_2. Only the right half of a meridional plane is shown. The vertical line to the left is the axis. A: $Re = 1000, h = 1.5, \gamma = -0.01$, no bubble. B_1: $Re = 2200, h = 2.0, \gamma = -0.01$, upper bubble only. B_2: $Re = 1900, h = 2.7, \gamma = 0.05$, middle bubble only. B_3: $Re = 2925, h = 3.6, \gamma = 0$, lower bubble only. C_1: $Re = 2250, h = 2.3, \gamma = -0.01$, top and middle bubbles. C_2: $Re = 2950, h = 3.5, \gamma = 0$, top and bottom bubbles. D: $Re = 2400, h = 2.7, \gamma = 0.05$, upper/middle bubble with inner structure. E: $Re = 2860, h = 3.4, \gamma = 0$, three bubbles. F: $Re = 2950, h = 3.4, \gamma = 0$, upper bubble and lower/middle bubble with inner structure.

Using this, (3.2) become

$$\dot{\rho} = \rho(a_{11} + a_{21}\rho + 2a_{12}z + \ldots), \tag{3.5a}$$

$$\dot{z} = -a_{10} - 2a_{20}\rho - a_{11}z - 3a_{30}\rho^2 - 2a_{21}\rho z - a_{12}z^2 - \ldots. \tag{3.5b}$$

If $a_{10} = 0$, the origin is a critical point for (3.5). Linearizing at the origin one obtains the system matrix

$$\mathbf{J} = \begin{pmatrix} a_{11} & 0 \\ -2a_{20} & -a_{11} \end{pmatrix}. \tag{3.6}$$

If $a_{11} \neq 0$, the origin is a hyperbolic saddle (or stagnation point) with eigenvalues $a_{11}, -a_{11}$. The separatrix corresponding to $-a_{11}$ is the centre axis, while the other
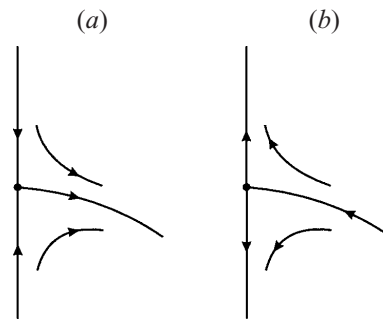
FIGURE 2. Flow near a regular critical point on the axis shown in (r, z) coordinates. (*a*) Separation, $a_{11} > 0$. (*b*) Attachment, $a_{11} < 0$.

separatrix is

$$z = -\frac{a_{20}}{a_{11}}\rho + O(\rho^2). \tag{3.7}$$

In terms of the original radial variable r, it follows that the dividing streamline is orthogonal to the centre axis. Depending on the sign of a_{11}, the point is either a point of separation or attachment. See figure 2.

If $a_{10} = a_{11} = 0$, the origin is a degenerate critical point because zero is an eigenvalue of $\boldsymbol{J}$ of algebraic multiplicity two. Two sub-cases must be treated individually. If $a_{20} \neq 0$, the geometric multiplicity m_g of the eigenvalue is one, and we call the degeneration simple. If $a_{20} = 0$, $m_g = 2$, the degeneracy is double. It turns out that we only need the first case here, and will briefly return to the latter case in §6.

When the linear part of a system of ordinary differential equation is degenerate, higher-order terms become decisive. We will simplify these terms by transforming the equations to normal form (Guckenheimer & Holmes 1983; Chow, Li & Wang 1994). First, quadratic terms are considered, and by a suitable choice of an almost-identity quadratic coordinate transformation as many quadratic terms as possible are removed. The terms which cannot be removed are the so-called resonant terms which, if non-zero, determine the qualitative behaviour of the streamlines. If these terms are also degenerate, cubic or higher-order terms must be computed by further transformations until some non-degeneracy condition is fulfilled. Furthermore, since we want to study the streamlines not only at the exact degeneracies, but with the coefficients a_{ij} taking values close to their degenerate value, we consider those as small parameters.

The detailed computations leading to the normal form can be found in Brøns (1999). The main result is (in a slightly different formulation)

THEOREM 3.1 (Normal form). *Let* $a_{10}, \ldots, a_{1\,N-1}$ *be small parameters. Assuming the non-degeneracy conditions* $a_{20} \neq 0, a_{1N} \neq 0$*, a normal form of order* N *for the stream function* (3.3) *is*

$$\psi = \rho(-\mu + \tfrac{1}{2}\sigma\rho + f(z)), \quad f(z) = \sum_{i=1}^{N} c_i z^i, \quad c_{N-1} = 0, \quad c_N = \frac{1}{N}, \tag{3.8}$$

where

$$\sigma = \begin{cases} -1 & \text{for } N \text{ even and } a_{20}/a_{1N} < 0, \\ +1 & \text{for } N \text{ even and } a_{20}/a_{1N} > 0 \text{ or } N \text{ odd,} \end{cases}$$

and μ *and* c_i, $i = 1, \ldots, N-2$ *are transformed small parameters.*
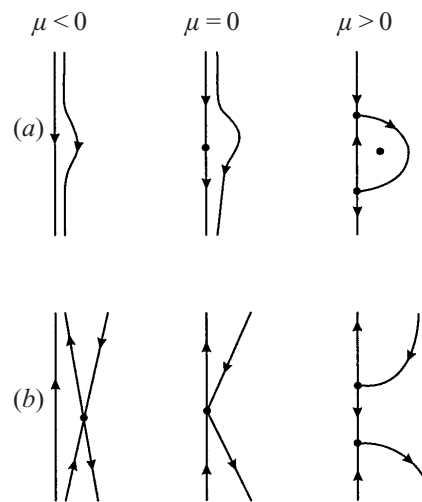
FIGURE 3. Streamline patterns in (r, z) coordinates for the second-order normal form equation (3.9). (a) $\sigma > 0$. (b) $\sigma < 0$.

For the understanding of multi-parameter bifurcation, the concept of *codimension* is important. Loosely speaking, the codimension of a bifurcation is the minimal number of parameters needed to described the bifurcation. From the normal form (3.8), the codimension is readily determined, since only the important, resonant, coefficients to a given order remain, and the rest are transformed away. Hence, the codimension of the bifurcation of the normal form of order N at $\mu = c_1 = \cdots = c_{N-2} = 0$ is $N - 1$.

If a dynamical system has p free parameters, one will generically find bifurcations of codimension up to p. For the rotating flow we will in §5.1 and §5.2 determine bifurcation diagrams for fixed values of γ and vary only Re, h. In these diagrams, we do not expect to (and indeed will not) find features from the normal forms of order higher than three. Here we briefly discuss the relevant cases.

For $N = 2$, the normal form equations for the streamlines are

$$\dot{\rho} = \rho z, \quad \dot{z} = \mu - \sigma\rho - \tfrac{1}{2}z^2. \tag{3.9}$$

The system has critical points on the axis given by $(\rho, z) = (0, \pm\sqrt{2\mu})$. There is also an off-axis critical point $(\rho, z) = (\sigma\mu, 0)$. Since $|\boldsymbol{J}| = 2\mu$ this point is a saddle for $\mu < 0$ and a centre for $\mu > 0$. The corresponding bifurcation diagrams are shown in figure 3. Physically, case (a) is the creation of a bubble on the axis. Case (b) will occur when two bubbles merge.

For $N = 3$, the normal form equations for the streamlines are

$$\dot{\rho} = \rho(c_1 + z^2), \quad \dot{z} = \mu - \rho - c_1 z - \tfrac{1}{3}z^3. \tag{3.10}$$

One easily obtains that bifurcation of critical points on the axis occurs when $\mu^2 = -\tfrac{4}{9}c_1^3$ and bifurcation of critical points off the axis occurs when $c_1 = 0, \mu < 0$. This results in the bifurcation diagram shown in figure 4. The bifurcation set consist of three curves of codimension-one bifurcations which meet at the codimension-two point at the origin. The bifurcation curve b_1 is the creation of a small bubble as in figure 3(a). The bifurcation curve b_2 is the merging of a small bubble with one end of a large bubble as in figure 3(b). The bifurcation curve b_3 is the creation/destruction of two critical points off the axis in a *cusp bifurcation*. In a general flow in a region not
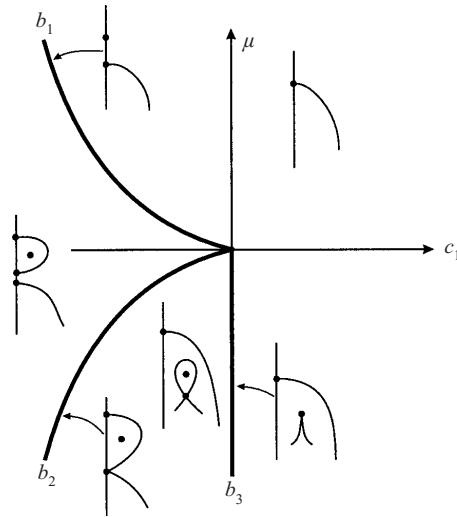
FIGURE 4. Bifurcation diagram for the third-order normal form equation (3.10).

containing any given streamlines or boundaries, this is the only possible bifurcation of codimension one (Brøns & Hartnack 1999).

4. Numerics

4.1. *Numerical location of bifurcation sets*

From a simulation we obtain ψ-values at the grid points in the numerical grid. A first task is to use these data to locate critical points on the axis, at, say, $(r, z) = (0, z_c)$.

Critical points on the axis are characterized by $w = 0$. From the definition of ψ

$$w(r,z) = -\frac{1}{r}\frac{\partial \psi}{\partial r}(r,z), \tag{4.1}$$

and by a Taylor expansion of ψ we get

$$\psi(\Delta r, z_c) = \psi(0, z_c) + \frac{\partial \psi}{\partial r}(0, z_c)\Delta r + \frac{1}{2}\frac{\partial^2 \psi}{\partial r^2}(0, z_c)\Delta r^2 + O(\Delta r^3). \tag{4.2}$$

Using the boundary conditions (3.1) in (4.2) we obtain

$$w(0, z_c) = -\frac{\partial^2 \psi}{\partial r^2}(0, z_c) \approx -\frac{2}{\Delta r^2}\psi(\Delta r, z_c). \tag{4.3}$$

Hence, we can locate critical points on the axis by locating zeros of $\psi_0(z) = \psi(\Delta r, z)$ along an axial z-line close to the axis. In the following we will always choose this line to be the axial grid-line next to the axis.

An example with two bubbles is shown in figure 5. Between the zeros ψ_0 has extrema, and a simple way to find bifurcations of critical points on the axis is to monitor the values of ψ_0 at these extrema. If $\psi_0(p_1)$ changes sign from the negative value as in figure 5 to a positive value, this corresponds to the destruction of the top bubble in a bifurcation as in figure 3(*a*) going from right to left. Likewise, a change of sign of $\psi(p_2)$ would destroy the lower bubble, while a change of sign of $\psi(p_3)$ would give rise to a bifurcation as in figure 3(*b*), and would result in one large bubble with inner structure, type *D*. If three bubbles are present, type *E*, yet an extremum p_4
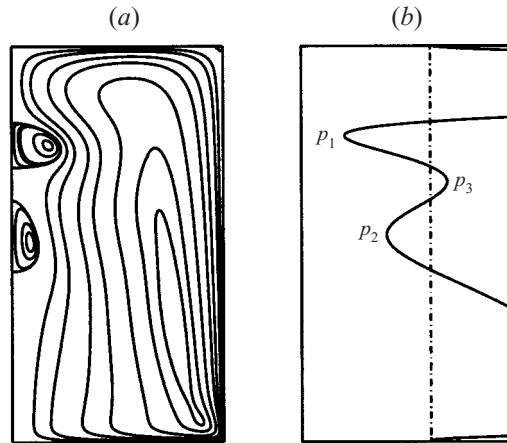
FIGURE 5. (*a*) Iso-curves of ψ for $Re = 2250$, $h = 2.3$, $\gamma = -0.01$. (*b*) Corresponding graph of $\psi_0(z) = \psi(\Delta r, z)$. The points p_1, p_2, p_3 are the extrema.
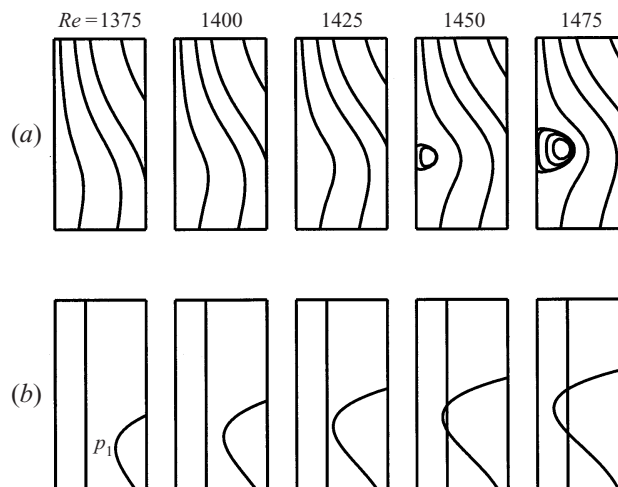

FIGURE 6. Creation of bubble at $h = 2$, $\gamma = 0$ for increasing values of Re as indicated. (*a*) Streamlines. (*b*) Corresponding graphs of $\psi_0(z)$. Only a small region of the flow domain is shown, $0 \leqslant r/R \leqslant 0.2$, $1 \leqslant z/R \leqslant 1.6$.

exists. A large set of plots like figure 5 for different values of the parameters can be found in Voigt (1998).

From a topological point of view the three cases B_1, B_2, B_3 are identical (as are C_1, C_2), since a bubble may move up and down the axis and change its shape and size continuously without any topological change. However, close to a bifurcation where a bubble appears a unique extremum p_i is associated with that bubble, and the extremum also exists when the bubble is not present as discussed above. Far from the bifurcation, when a certain bubble does not exist, the corresponding extremum may also not exist. Then the sub-classification makes no sense and should be interpreted carefully. The bubbles can only be distinguished when a sufficient number of p_i exist to label the bubbles uniquely.

To illustrate how the creation of a bubble can be monitored by ψ_0 we show a series of simulations for increasing Re in figure 6. This is a transition from type A to

B_1 (figure 1) with only one minimum p_1 of ψ_0. It is clearly seen that the minimum changes sign for Re between 1425 and 1450, and that a bubble is also created in the process.

To obtain a bifurcation set for a fixed value of γ for the bifurcation of the top bubble we approximate the dependence of $\psi_0(p_1)$ on the physical parameters by a quadratic expression,

$$\psi_0(p_1) = \mathscr{C}(h, Re) = c_{00} + c_{10}h + c_{01}Re + c_{20}h^2 + c_{02}Re^2 + c_{11}hRe. \qquad (4.4)$$

The six coefficients in (4.4) are determined by a least-squares fit. That is, for K simulations at different parameter values h_i, Re_i the corresponding value $\psi^{(i)}$ of ψ at p_1 is found, and the sum

$$\sum_{i=1}^{K}(\mathscr{C}(h_i, Re_i) - \psi^{(i)})^2 \qquad (4.5)$$

is minimized. The bifurcation set is then found as $\mathscr{C}(h, Re) = 0$. We proceed similarly for the other extrema. Values of K used are between 12 and 33.

In this way all bifurcations involving critical points on the axis can be found. In principle, a similar approach could be used to find cusp bifurcations of critical points off the axis, for instance by monitoring the distance between the two critical points involved in the bifurcation or the difference in the values of ψ at these points. We have, however, not been successful in this. First, locating critical points off the axis automatically is not a simple matter since an extremum of a two-variable function must be found (some possible strategies are discussed by Yeckel 1998). Second, for the critical points on the axis the bifurcation curve is determined by interpolation since both negative and positive values of $\psi(p_i)$ are available. For the cusp bifurcation any of the variables we suggest monitoring are defined only on one side of the bifurcation, so the bifurcation curve is determined by extrapolation. It is our experience that this difference results in a need for data points which are very close to the bifurcation. Locating such points requires many simulations and this makes the procedure very tedious.

We have chosen to approach the cusp bifurcations in a rather straightforward way. By visual inspection of the streamline pattern from a simulation close to a cusp bifurcation it was decided whether two critical points had merged or not. A bifurcation point is then determined as the mean value of two sufficiently close pairs of parameters for which the simulations are of distinct types. The bifurcation curve is obtained by connecting such points by a spline.

4.2. *Numerical accuracy*

The accuracy of the Navier–Stokes solver employed has in earlier studies been checked against measurements of the flow in a closed cylindrical container with one rotating end-cover. For the case of $h = 2$ and $\gamma = 0$ comparisons with visualizations (Sørensen & Christensen 1995), LDA measurements (Sørensen & Loc 1989) and PIV measurements (Westergaard, Buchhave & Sørensen 1993) showed that a grid resolution of $\Delta r = \Delta z = 0.01$, corresponding to a discretization of $N_r \times N_z = 101 \times 201$, gave results within experimental accuracy. To quantify the accuracy by which critical points are detected using the technique proposed in the previous subsection we here present results for three different grids consisting of 80×160, 100×200 and 150×250 mesh cells, referred to as coarse mesh, medium mesh and fine mesh, respectively. The test is carried out for the flow in a container with aspect ratio $h = 2$ and $\gamma = 0$ for which we look for the appearance of the first recirculation bubble. In figure 7 we
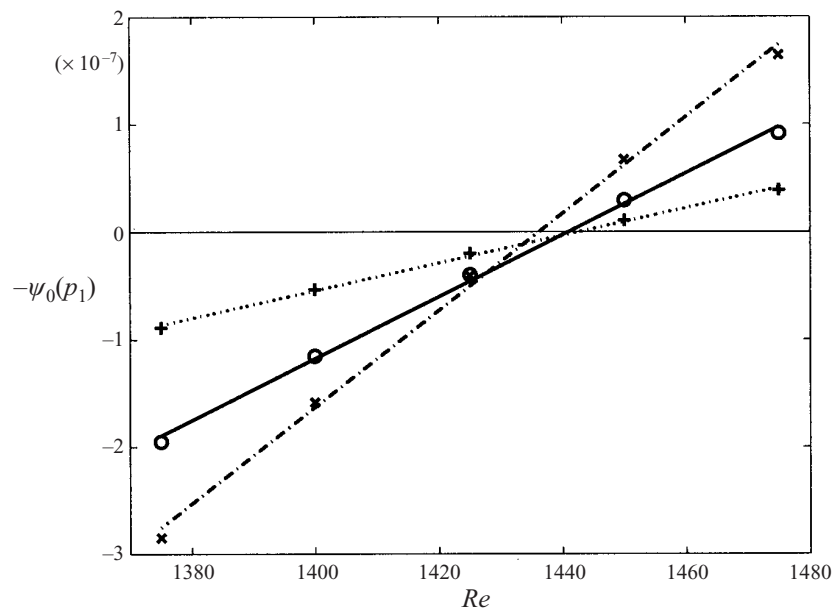
FIGURE 7. Comparisons between $\psi_0(p_1)$ for different grid sizes. The symbols show simulations used for least-squares fit shown as lines: $\times$, coarse mesh; $\bigcirc$, medium mesh; $+$, fine mesh.

depict the minimum value of the stream function on the first grid line off the axis, $-\psi_0(p_1)$, as function of Reynolds number for the three grids. When $-\psi_o(p_1)$ changes sign a bubble is born. From the figure it is seen that, independent of the number of grid points, in an interval of $\Delta Re = 100$, the quantity $-\psi_0(p_1)$ varies linearly as a function of the Reynolds number. The curves for the three grids intersect the zero line at $Re = 1436$, $Re = 1441$ and $Re = 1443$ for the coarse mesh, the medium mesh and the fine mesh, respectively. Using the interpolation technique described in §4.1 the bubble is created at $Re = 1414$ (see the diagram in figure 8), hence the dispersion amounts to about $\Delta Re = 30$. It appears from figure 8 that most of the data used to obtain the fit are from simulations at parameter values away from the bifurcation point at $h = 2$ and hence the accuracy of the interpolation is expected to be worst in this part of the bifurcation diagram.

Based on the results from the validation study and earlier works we conclude that a grid resolution of $\Delta r = \Delta z = 0.01$ is sufficient, and that the dispersion of the proposed interpolation technique is about $\Delta Re = 30$ in the worst case and in most other cases, depending on the number of computations in the parameter range of interest, it is much better.

5. Results

5.1. *The two-bubble regime*

In figure 8 we show the bifurcation diagram for $\gamma = 0$ obtained with the method described in §4.1 together with points marking the parameter values where simulations were used to obtain the least-squares fit of the bifurcation curves. No cusp bifurcations are observed. The same bifurcation curves are shown in figure 9 together with experimental data.

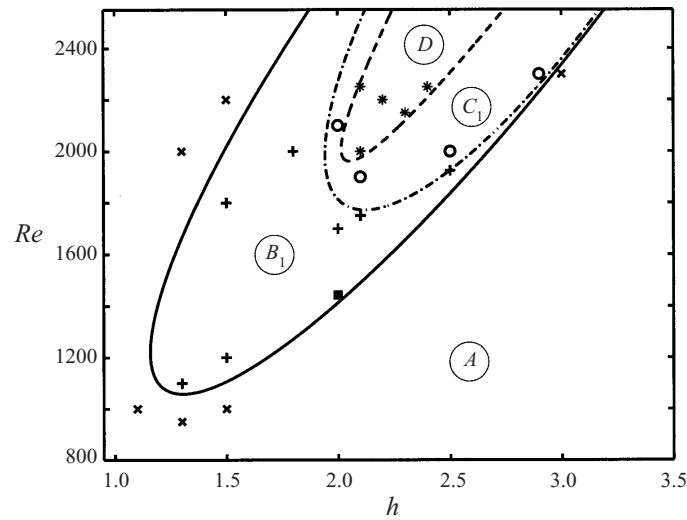A good agreement between numerical results and experiments is achieved, and it

FIGURE 8. Bifurcation diagram for $\gamma = 0$ involving up to two bubbles. The letters refer to the classification in figure 1. The symbols show parameter values where simulations were performed. ×, No bubbles, type A. +, Top bubble only, type B_1. ○, Top and middle bubbles, type C_1. *, upper/middle bubble with inner structure, type D. ■, Top bubble creation point obtained for $h = 2$ with variation of Re, figure 7, using the standard (medium) mesh. The curves show the bifurcation curves obtained from quadratic fits as described in the text. ——, Creation of top bubble; — · —, creation of middle bubble; — — —, merging of upper and middle bubble to one bubble with inner structure.
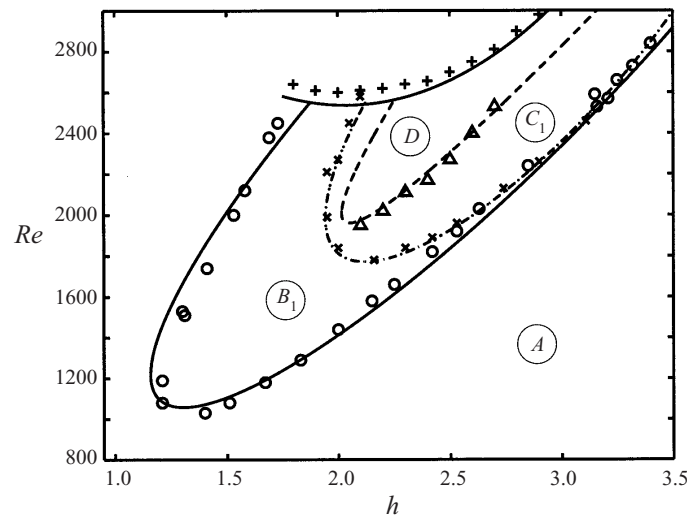

FIGURE 9. Bifurcation curves from figure 8 compared with experimental results. ○, Creation of upper bubble; ×, creation of middle bubble (both from Escudier 1984). △, Merging of two bubbles to one bubble with inner structure, from (Roesner 1989). +, Stability limit found by Escudier (1984). The corresponding line is a spline fit of the numerically determined stability limits.

appears that the agreement is best in the areas where the simulations are performed. The curves where the top and middle bubble are created are very close for h around 3. Escudier (1984) indicated that the curves actually cross for $h \approx 2.7$, and that the middle bubble is created for slightly lower Re than the upper bubble for high values
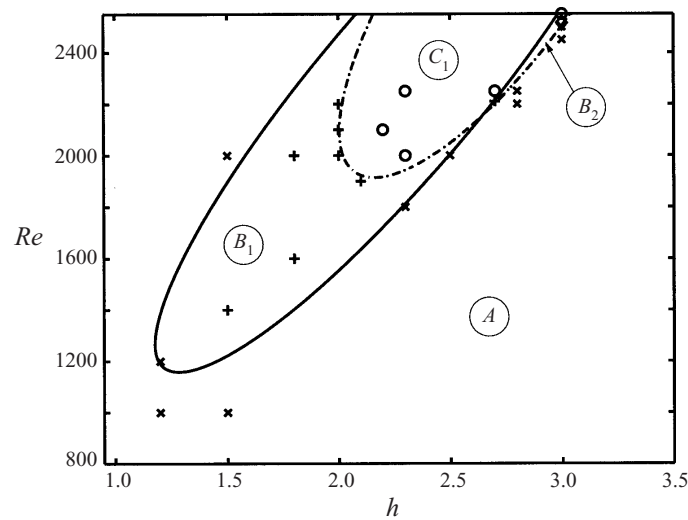
FIGURE 10. As figure 8, but for $\gamma = -0.01$. ◇, States with one lower bubble, type B_2.

of h. We have encountered crossings of the curves if fewer points are used in the fit, but it has not been possible to obtain this topology numerically. Obviously, this is a very sensitive feature of the bifurcation diagram which we have not resolved completely, but we believe that the topologies of type B_2 cannot occur for $\gamma = 0$.

While Escudier (1984) reported that the two bubbles can merge into one large bubble with inner structure, he did not include the associated bifurcation curve in his diagram. Roesner (1989) did indicate this curve in his corresponding diagram, and as shown in figure 9 our results are in good agreement. However, Roesner continued the bifurcation curve through the data to end at the bifurcation curve for the creation of the middle bubble. This is not possible according to the topological analysis in §3, and we find that the bifurcation curve turns around before it reaches the middle bubble curve. For the upper branch of the bubble merging curve no experimental data are available, but the present approach shows that this part must exist.

Finally, we have added comparisons of the stability limit in figure 9. The numerical curve is determined from the assumption that the transition to unsteady flow is through a supercritical Hopf bifurcation. The curve is a fit by a natural spline through four points determined as suggested by Daube & Sørensen (1989): for fixed h we find the square of amplitude of the fluctuation in the arbitrarily chosen grid points $(30, 30)$, $(50, 50)$ and $(70, 70)$ for three slightly supercritical values of Re. For each grid point the square of the amplitude of the fluctuation is linearly dependent on Re. Using a least-squares fit an analytical expression is obtained and extrapolation to zero leads to the critical value of Re for each grid point. The critical Reynolds number is now found as the mean value of the critical Reynolds number for each grid point.

Again good agreement is obtained. The topology bifurcation curves are stopped at the stability limit since they are derived under the assumption of a steady flow.

Numerical results for a slightly counter-rotating lid with $\gamma = -0.01$ are shown in figure 10. The upper and middle bubble creation curves have become narrower and have moved slightly upwards to the right. The curves also have different relative position and now a topology of type B_2 is definitely possible. The bubble merging curve, however, has moved completely out of the region. We have not done any

M. Brøns, L. K. Voigt and J. N. Sørensen
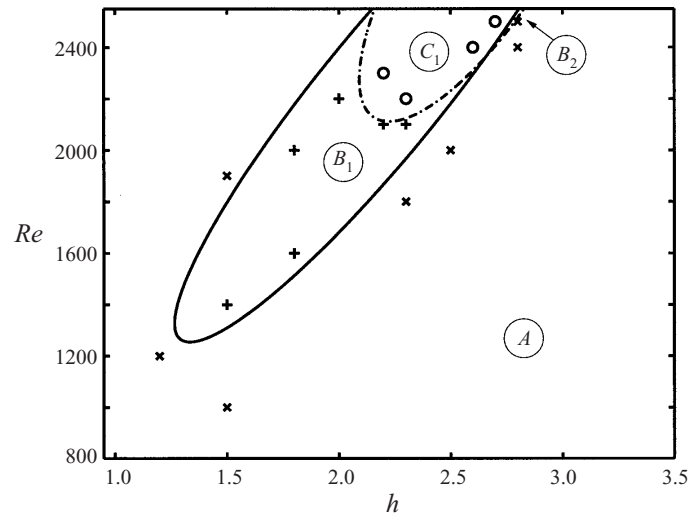
FIGURE 11. As figure 8, but for $\gamma = -0.02$.
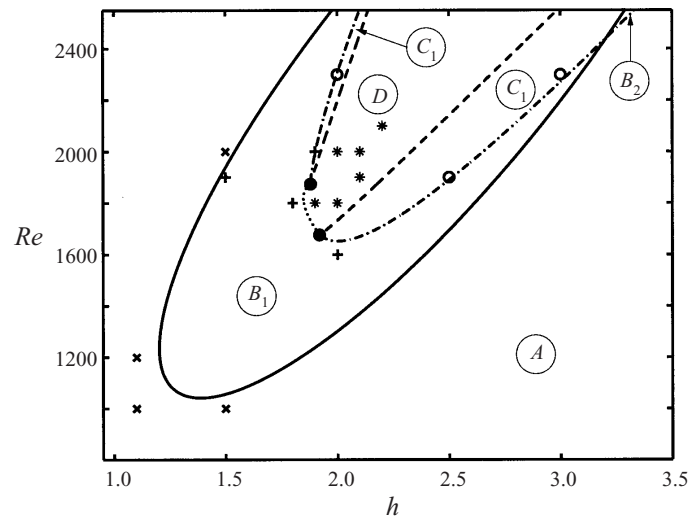
FIGURE 12. As figure 8, but for $\gamma = 0.01$. ●, Codimension-two bifurcation points.
$\cdots\cdots$, Spline fit of cusp bifurcation curve.

computations of the stability limits for this and the following cases in this section. However, numerical computations by Gelfat *et al.* (1996*b*) show that for $h = 1.5$ the stable region is minimal for γ very close to zero, and that in the γ-range considered here the stable region grows rapidly when γ is moved away from zero. The region depicted in figures 10–13 is definitely below the stability limit.

Further decreasing γ to -0.02, figure 11, we find essentially the same tendencies. The bifurcation curves have moved further upward and to the right, and have become even narrower. The diagram shows a small region with a topology of type B_2, one middle bubble only. Its existence cannot be verified within the computational accuracy, and we have not found this type of flow in simulations.

For positive values of γ we observe the opposite tendencies. As γ is increased, the
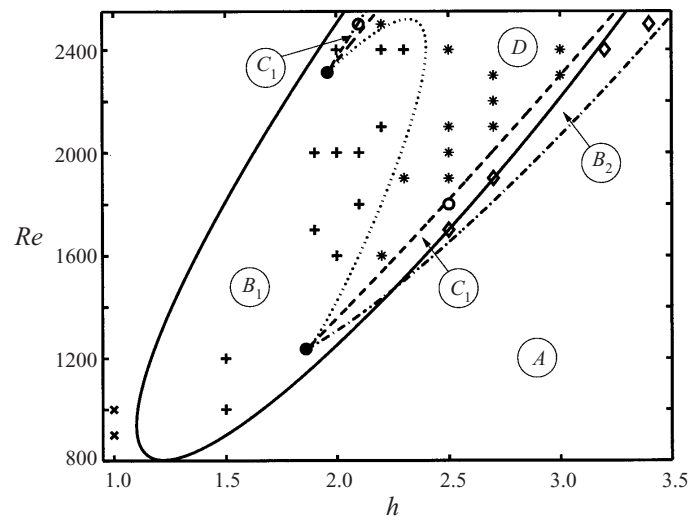
FIGURE 13. As figure 12, but for $\gamma = 0.05$. $\diamond$: States with one middle bubble, type B_2.

bubble merging curve moves towards the middle bubble creation curve. At some value of γ just below 0.01 they touch tangentially and a further increase of γ results in the creation of two codimension-two points as shown for $\gamma = 0.01$ in figure 12. From the theory in § 3 we know that from such points three bifurcation curves emanate. Here the codimension-two points are determined as intersections of the two quadratic curves of top and middle bubble creation. The third curve, a cusp bifurcation curve, is constructed as a spline connecting these two points as described in § 4.1. If the parameters are varied across this curve, a direct transition from topology of type B_1 to type D is possible. In this process the top bubble first grows as the bottom saddle point moves downwards along the axis before the inner structure is created in a cusp bifurcation. The diagram shows a small region with a topology of type B_2. As for $\gamma = -0.02$, computational accuracy does not allow us to decide whether this really exists.

Further increasing γ to 0.05, figure 13, the two codimension-two points move further away and the connecting cusp bifurcation curve goes to high values of Re and h.

For increasing positive rotation ratios the lower codimension-two point moves towards the middle bubble creation curve. A parameter set where the point has moved onto the curve will be a bifurcation point of codimension three and hence describes the most complicated bifurcation locus that can possibly appear in this setting. The associated bifurcation diagram with $N = 4$ is shown in Brøns (1999) and is not difficult to find from the normal form (3.8). We have not pursued whether such a point actually exists, but there is no doubt that for higher values of γ the bifurcation diagram is qualitatively different, and becomes much richer. The simulations by Gelfat *et al.* (1996*b*) show that the bubbles on the axis may creep around the top corner and attach to the upper lid and further interact with the bubble coming from the upper right corner, small but clearly visible in figure 1, B_2 and D. These bifurcations are not covered in the present paper.

5.2. *The three-bubble regime for $\gamma = 0$*

Escudier (1984) observed a narrow parameter region for $\gamma = 0$ with three recirculation bubbles. In his original (h, Re) bifurcation diagram this is shown as a narrow wedge-
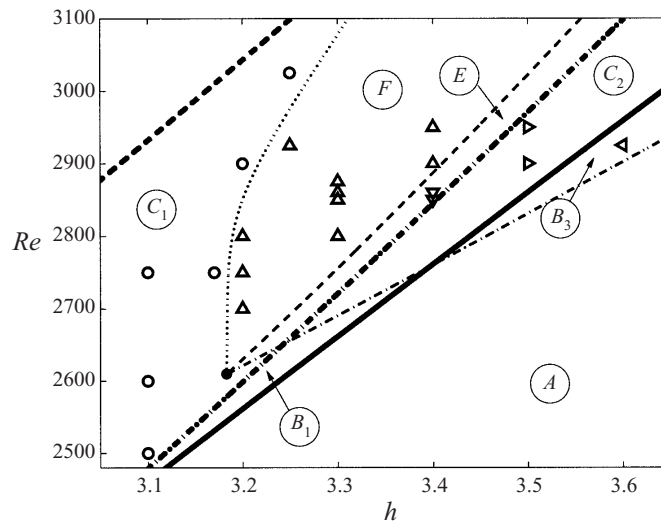
FIGURE 14. Bifurcation diagram for the three-bubble region for $\gamma = 0$. The symbols show parameter values where simulations are performed. $\bigcirc$, Top and middle bubbles, type C_1. $\triangleleft$, Lower bubble only, type B_3. $\triangleright$, Top and lower bubble, type C_2. $\triangledown$, Three bubbles, type E. $\triangle$, Top bubble and lower bubble with inner structure, type F. The curves show the bifurcation sets obtained from fits of the data. The heavy curves are the two-bubble curves from figure 8. The light curves are the curves involving the lower bubble. $- \cdot -$, creation of lower bubble; $- - -$, merging of middle and lower bubble to one bubble with inner structure; $\cdots\cdots$, cusp bifurcation in middle/lower bubble.

shaped region with open ends just above the lower bubble creation curve for h approximately between 3.25 and 3.4 and Re between 2800 and 2950.

Proceeding as before we have found the bifurcation curve corresponding to the creation of the third, lower, bubble. Additionally, we have found that the lower bubble may interact with the middle bubble and create a bubble with inner structure. These two curves meet in a codimension-two point, and from the bifurcation theory of §3 we know that further a cusp bifurcation curve must emanate from this point. The latter curve is approximated with a spline, and the complete diagram for this region is shown in figure 14. The bifurcation curves corresponding to the creation of the top and middle bubbles are based on fits from the points in the new diagram only and hence do not agree exactly with the curves in figure 8. We do not compare with experiments since very few data are available in this region and the bifurcation curves are closer than the experimental resolution.

The bifurcation structure of the three-bubble regime has to our knowledge not been studied in any detail before. Note that it has a well-defined lower end at the codimension-two point at approximately $(h, Re) = (3.2, 2600)$. This gives rise to a larger region than found by Escudier (1984) who also indicates that the region ends before the stability limit. Our analysis suggests that the region is open towards the higher values of the parameters.

We believe that the bifurcation diagrams obtained here for $\gamma = 0$ are complete. Some of the parameter regions are so small and with very small bubbles so it may be difficult to verify them experimentally.

6. Conclusions

The analysis of the present paper shows that the cylinder flow is very sensitive to variation of the rotation ratio. However, all observed bifurcations can be completely described using the normal forms for a simple linear degeneracy. These are based on the non-degeneracy condition $a_{20} \neq 0$ in the Taylor expansion (3.3), that is, $\partial^4 \psi / \partial r^4 \neq 0$ at the critical points on the axis. From a mathematical point of view there is no way to rule out critical points with a double degeneracy *a priori*, and bifurcations associated with this may certainly occur in other rotating flows with vortex breakdown. The study of such bifurcations is complicated by the fact that normal form transformations as used here do not yield any simplifications. Some simplifications can be obtained as shown by Hartnack (1999) in a similar analysis for the flow close to a wall, but a much richer set of bifurcations occur. For the normal form equation (3.8) saddle points on and off the axis cannot be connected by dividing streamlines (separatrices) in a heteroclinic loop: for critical points off the axis one finds $\psi = -\frac{1}{2}\sigma\rho^2 \neq 0$, while critical points on the axis have $\psi = 0$. This restriction does not apply in the double-degenerate case where global streamline bifurcations occur when heteroclinic connections are broken.

We have combined bifurcation theory for dynamical systems and numerical simulations to obtain a classification of the steady patterns in the flow. Dynamical systems theory provides the building blocks from which the bifurcation diagrams are constructed. Although our results are of a quantitative nature, we have not aimed at a very precise numerical determination of the bifurcation sets, but primarily at a correct qualitative picture. This is obtained with a very limited number of simulations – an important feature of the method, since computing time is a serious constraint, in particular for the larger grids for high h and close to the stability limit where transients are very long. To obtain higher accuracy, the use of global quadratic fitting of bifurcation curves can be refined to higher orders or local fits using e.g. splines, and the analysis can immediately be extended to get a complete overview of the entire range of interest, $-1 \leqslant \gamma \leqslant 1$.

The classification of streamline topologies of vortex breakdown is by no means exhausted. Here we have only been concerned with bubble-type breakdown, and not with the spiral-type, see e.g. Leibovich (1984). A topological approach seems a promising way to shed further light on qualitative aspects of the vortex breakdown and may be a useful guide in the interpretation of visualization experiments.

REFERENCES

BAKKER, P. G. 1991 *Bifurcations in Flow Patterns*. Dordrecht: Klüwer.

BAR-YOSEPH, P. Z., SOLAN, A. & ROESNER, K. G. 1990 Sekundärstömung in axialsymmetrichen Hohlräumen. *Z. Angew. Math. Mech.* **70**, T442–T444.

BRØNS, M. 1994 Topological fluid dynamics of interfacial flows. *Phys. Fluids* **6**, 2730–2737.

BRØNS, M. 1999 Topological fluid mechanics of axisymmetric flows. In *Simulation and Identification of Organized Structures in Flows* (ed. J. N. Sørensen, E. J. Hopfinger & N. Aubry), pp. 213–222. Dordrecht: Klüwer.

BRØNS, M. & HARTNACK, J. N. 1999 Streamline topologies near simple degenerate critical points in two-dimensional flow away from boundaries. *Phys. Fluids* **11**, 314–324.

CHOW, S.-N., LI, C. & WANG, D. 1994 *Normal Forms and Bifurcation of Planar Vector Fields*. Cambridge University Press.

Daube, O., Loc, T. P., Monet, P. & Coutanceau, M. 1985 Ecoulement instationaire décollé d'un fluide incompressible autour d'un profil: une comparaison theorié-experience. *AGARD CP* 366.

Daube, O. & Sørensen, J. N. 1989 Simulation numerique de l'ecoulement periodique axisymmetrique dans une cavite cylindrique. *C. R. Acad. Sci. Paris* (2) **308**, 463–469.

Escudier, M. P. 1984 Observations of the flow produced in a cylindrical container by a rotating endwall. *Exps. Fluids* **2**, 189–196.

Gelfat, A. Y., Bar-Yoseph, P. Z. & Solan, A. 1996a Stability of confined swirling flow with and without vortex breakdown. *J. Fluid Mech.* **311**, 1–36.

Gelfat, A. Y., Bar-Yoseph, P. Z. & Solan, A. 1996b Steady states and oscillatory instability of swirling flow in a cylinder with rotating top and bottom. *Phys. Fluids* **8**, 2614–2625.

Guckenheimer, J. & Holmes, P. 1983 *Nonlinear Oscillations, Dynamical Systems, and Bifurcations of Vector Fields*. Springer.

Hartnack, J. N. 1999 Streamline topologies near a fixed wall using normal forms. *Acta Mechanica* **136**, 55–75.

Hunt, J. C. R., Abell, C. J., Peterka, J. A. & Woo, H. 1978 Kinematical studies of the flow around free or surface-mounted obstacles; applying topology to flow visualization. *J. Fluid Mech.* **86**, 179–200.

Jahnke, C. C. & Valentine, D. T. 1998 Recirculation zones in a cylindrical container. *Trans. ASME J. Fluids Engng* **120**, 680–684.

Leibovich, S. 1984 Vortex stability and breakdown: Survey and extension. *AIAA J.* **22**, 1192–1206.

Lopez, J. M. 1990 Axisymmetric vortex breakdown part 1. Confined swirling flow. *J. Fluid Mech.* **221**, 533–552.

Lopez, J. M. & Perry, A. D. 1992 Axisymmetric vortex breakdown. Part 3. Onset of periodic flow and chaotic advection. *J. Fluid Mech.* **234**, 449–471.

Perry, A. E. & Chong, M. S. 1987 A description of eddying motions and flow patterns using critical-point concepts. *Ann. Rev. Fluid Mech.* **19**, 125–155.

Roesner, K. G. 1989 Recirculation zones in a cylinder with rotating lid. In *Proc. IUTAM Symp. on Topological Fluid Mechanics* (ed. A. Tsinober & H. K. Moffatt), pp. 699–708. Cambridge University Press.

Ronnenberg, B. 1977 Ein Selbstjustierendes 3-komponenten-Laserdoppler-anemometer nach dem Vergleichsverfaren, angewandt auf Untersuchungen in einer stationären zylindersymmetrischen Drehströmung mit einem Rückströmgebiet. *Bericht* 19. Max-Planck-Institut für Strömungsforschung, Göttingen.

Sørensen, J. N. & Christensen, E. A. 1995 Direct numerical simulation of rotating fluid flow in a closed cylinder. *Phys. Fluids* **7**, 764–778.

Sørensen, J. N. & Loc, T. P. 1989 High-order axisymmetric Navier–Stokes code: Description and evaluation of boundary conditions. *Intl J. Numer. Meth. Fluids* **9**, 1517–1537.

Sotiropoulos, F. & Ventikos, Y. 1998 Transition from bubble-type vortex breakdown to columnar vortex in a confined swirling flow. *Intl J. Heat Fluid Flow* **19**, 446–458.

Spohn, A., Mory, M. & Hopfinger, E. J. 1993 Observations of vortex breakdown in an open cylindrical container with a rotating bottom. *Exps. Fluids* **14**, 70–77.

Spohn, A., Mory, M. & Hopfinger, E. J. 1998 Experiments on vortex breakdown in a confined flow generated by a rotating disc. *J. Fluid Mech.* **370**, 73–99.

Tobak, M. & Peake, D. J. 1982 Topology of three-dimensional separated flows. *Ann. Rev. Fluid Mech.* **14**, 61–85.

Tsitverblit, N. 1993 Vortex breakdown in a cylindrical container in the light of continuation of a steady solution. *Fluid Dyn. Res.* **11**, 19–35.

Vogel, H. U. 1968 Experimentelle Ergebnisse über die laminäre Strömung in einem zylindriche Gehäuse mit darin rotierender Scheibe. *Bericht* 6. Max-Planck-Institut für Strömungsforschung, Göttingen.

Voigt, L. K. 1998 Theoretical and computational description of vortex structures in a cylinder with rotating top and bottom. Master's thesis, Department of Mathematics, Technical University of Denmark.

Westergaard, C., Buchhave, P. & Sørensen, J. N. 1993 PIV measurements of turbulent and chaotic structures in a rotating flow using an optical correlator. In *Laser Techniques and Applications in Fluid Mechanics* (ed. R. J. Adrian). Springer.

Yeckel, A. 1998 Tools for parameter studies in fluid dynamics. *Intl J. Numer. Meth. Fluids* **28**, 1199–1216.